

Correlated spectrum of distant semiconductor qubits coupled by microwave photons

Bao-Chuan Wang^{1,2†}, Ting Lin^{1,2†}, Hai-Ou Li^{1,2†}, Si-Si Gu^{1,2}, Ming-Bo Chen^{1,2}, Guang-Can Guo^{1,2}, Hong-Wen Jiang³, Xuedong Hu⁴, Gang Cao^{1,2*}, Guo-Ping Guo^{1,2,5*}

1. CAS Key Laboratory of Quantum Information, University of Science and Technology of China, Hefei, Anhui 230026, China
2. CAS Center for Excellence in Quantum Information and Quantum Physics, University of Science and Technology of China, Hefei, Anhui 230026, China
3. Department of Physics and Astronomy, University of California at Los Angeles, California 90095, USA
4. Department of Physics, University at Buffalo, SUNY, Buffalo, New York 14260-1500, USA.
5. Origin Quantum Computing Company Limited, Hefei, Anhui 230026, China

†These authors contributed equally to this work.

*Corresponding author. Email: gcao@ustc.edu.cn (G.C.); gpguo@ustc.edu.cn (G.-P.G.)

ABSTRACT

Circuit quantum electrodynamics (QED) provides a promising gateway towards nonlocal qubit interactions and non-demolition qubit read-out for scalable quantum computation. Recently, strong coupling of two semiconductor qubits by a microwave resonator has been convincingly demonstrated. Here, we develop a new spectroscopic method to quickly and intuitively characterize the correlations of two microwave-photon-coupled semiconductor qubits. Nine different coupling regimes can be conveniently identified via reflectometry of a high-impedance resonator. In particular, highly distinctive and unique geometric patterns are revealed as we tune the qubit tunnel couplings relative to the frequency of the mediating photons. These observed patterns are in excellent agreement with a simulation of the input-output response of the microwave resonator using the Tavis-Cummings model, and allow us to readily identify different parameter regimes for both qubits. This correlated spectroscopy method could potentially be expanded as a practical method for quickly characterizing multiple cavity QED coupled semiconductor qubits.

INTRODUCTION

Semiconductor quantum dots, which are compatible with conventional manufacturing technology, are a promising candidate for scalable quantum computing (1-3). In semiconductor systems, significant progress has been made over the past decade (4-20). However, as the number of qubits increases (5, 21, 22), the coupling of arbitrary pairs of distant qubits and the characterization of coupled qubits remain outstanding challenges.

With the implementation of cavity QED architecture, photons in a microwave resonator have proven to be an effective medium in coupling distant quantum systems ranging from superconducting qubits to spin ensembles (23-25). Meanwhile, photon-qubit interaction also provides an efficient tool for quantum control and measurement of qubits (26-29). In semiconductor systems, a series of pioneering works has been performed to explore coupling of quantum dots with a microwave resonator (30-36). Recently, benefiting

from the application of a high-impedance microwave resonator and an improvement in the qubit lifetime, strong coupling, where the coupling rate g between the qubit and the photon exceeds both the qubit's decoherence rate γ_2 and the photons' decay rate κ_{tot} (23, 24), has been demonstrated via observation of vacuum Rabi mode splitting in the frequency domain for both spin and charge qubits based on semiconductor quantum dots (37-41). Consequently, the milestones for nonlocal semiconductor qubit-qubit interactions in the strong coupling limit have been reached (42, 43).

Here, we fabricate two semiconductor qubits strongly coupled with a high-impedance resonator (37, 42) and study the correlated two-qubit spectrum. In contrast with earlier explorations where probe frequency is varied relative to the qubit frequencies (37, 38, 44, 45), here we tune the qubit operation frequencies electrically (via the gate voltages for the quantum dots) while keeping the probe frequency constant. We measure the microwave response of the two coupled qubits at the cavity resonance frequency while scanning the detuning of both qubits, producing a correlated spectrum of the two coupled qubits. We then explore the evolution of this correlated spectrum as we vary the tunnel coupling strengths for both qubits. Our systematic study reveals distinctive geometric patterns in the spectrum for each parameter regime, and we can establish a one-to-one correlation between these geometric features and the system parameters. Using the Tavis-Cummings (TC) model (44), we simulate the correlated spectrum and find excellent agreement with our experimental results. Our results clearly demonstrate that, with our spectroscopy method, pairwise correlations between nonlocal semiconductor qubits can be characterized quickly and intuitively.

RESULTS

As shown in Fig. 1A, our device consists of two conventional gate-defined double quantum dots (DQDs) and a $\lambda/4$ superconducting quantum interference device (SQUID) array resonator fabricated on a GaAs/AlGaAs heterostructure. The left and right DQDs encoding the two distant qubits are defined by applying suitable gate voltages to surface metal gates, denoted as DQD 1 and DQD 2, respectively. The interdot tunnel coupling $2t_{1(2)}$ can be tuned with gates 1MU (2MU) and 1MD (2MD). Gates 1BL (2BL) and 1BR (2BR) control the detuning $\delta_{1(2)}$ between the left dot and right dot of DQD 1(2), respectively. The gate voltages applied to gates 1PL and 2PR are kept constant in this experiment.

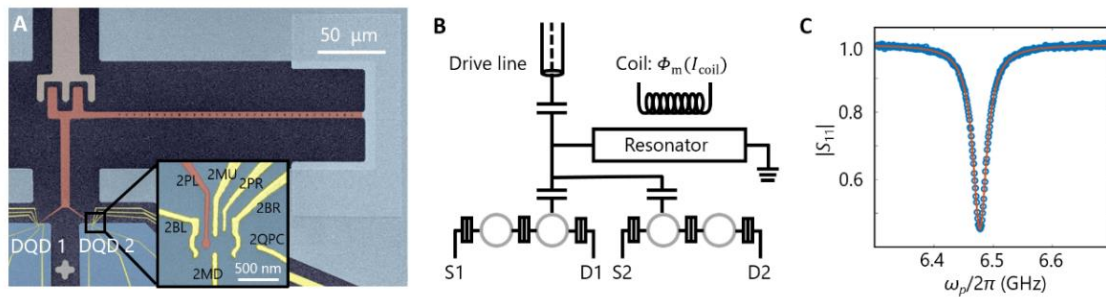


Fig. 1. Sample and simplified circuit diagram. (A) False-color electron micrograph of our hybrid device. The SQUID array resonator (red) is capacitively coupled with the drive line (cream) and two DQDs. A coil is mounted above the device to adjust the resonator frequency by changing the flux current. The inset in (A) shows an enlarged view of the right DQD (DQD 2). Gates 2BL, 2MU, 2PR, 2BR and 2MD (yellow) are used to define DQD 2, and gate 2PL (red) is connected to the resonator. (B) The simplified circuit diagram of (A) shows that the frequency tunable resonator is capacitively coupled with the drive line and both DQDs. The probe

microwave is applied to the hybrid system through the drive line. The input microwave and the reflected microwave are separated by a circulator (not shown). (C) Measured resonator reflectance spectrum (blue circles) as a function of the probe microwave frequency $\omega_p/2\pi$, displaying a dip at the resonator resonance frequency $\omega_r/2\pi = 6.48$ GHz. The solid line is the fitting result using input-output theory with $(\kappa_{int}, \kappa_{ext}, \kappa_{tot})/2\pi = (9.60, 25.46, 35.06)$ MHz.

By replacing the center metal conductor of the superconducting coplanar waveguide (CPW) resonator with an array of high-inductance SQUIDs, we implement a high-impedance $\lambda/4$ SQUID array resonator [red in Fig. 1A] with $Z_r \sim 1$ k Ω (37) which far exceeds the typical 50 Ω impedance of a traditional superconducting CPW resonator, enabling the realization of strong coupling between the qubits and the resonator. At the voltage antinode of the electric field, the SQUID array resonator extends two metal gates (gate 1PR and gate 2PL) to couple the two DQDs [red gate of DQD 1 in the inset of Fig. 1A]. On the other hand, the resonator is capacitively coupled to the drive line [cream in Fig. 1A] with interdigital capacitors. The device can be simplified into a circuit diagram, as shown in Fig. 1B.

The unloaded resonator is characterized by measuring the microwave reflectance $|S_{11}|$. As illustrated in Fig. 1B, microwave with frequency $\omega_p/2\pi$ generated by a vector network analyzer (VNA) is applied to the SQUID array resonator through the drive line. After being reflected from the hybrid system, the signal is separated from the input by a circulator placed in front of the drive line and detected by the VNA.

For a reflecting $\lambda/4$ resonator, the reflectance amplitude $|S_{11}|$ is minimum when the probe microwave is resonant with the resonator: $\omega_p = \omega_r$; i.e., a dip appears in the resonator spectrum [Fig. 1C]. Fitting the reflectance spectrum with input-output theory, we determine the resonator's internal loss rate, external coupling rate and total loss linewidth as $(\kappa_{int}, \kappa_{ext}, \kappa_{tot})/2\pi = (9.60, 25.46, 35.06)$ MHz at $\omega_r/2\pi = 6.48$ GHz, which we use in the following experiments.

Theoretically, our hybrid system of two two-level atoms interacting with a cavity can be described by the Tavis-Cummings (TC) model of cavity QED theory with the Hamiltonian (44)

$$H_{TC} = \omega_r a^\dagger a + \frac{1}{2}(\omega_{a,1} \sigma_{z,1} + \omega_{a,2} \sigma_{z,2}) + [g_1(\sigma_{+,1} a + a^\dagger \sigma_{-,1}) + g_2(\sigma_{+,2} a + a^\dagger \sigma_{-,2})], \quad (1)$$

where we have set $\hbar = 1$. The first two terms are for a free resonator and two independent charge qubits. The resonator frequency is $\omega_r/2\pi$. And a^\dagger (a) creates (annihilates) a photon. The charge qubit transition (operation) frequencies are $f_{a,i} = \omega_{a,i}/2\pi = \sqrt{\delta_i^2 + (2t_i)^2}$, where δ_i and $2t_i$ are the detuning and tunnel coupling, respectively. The Pauli matrices $\sigma_{z,i}$ and $\sigma_{+/-,i}$ are defined in the charge qubit eigenbasis. The last term gives the interactions between DQD i and the resonator with coupling rate (37, 38, 45)

$$g_i = g_i^{max} \frac{2t_i}{\sqrt{(2t_i)^2 + \delta_i^2}} \quad (2)$$

According to input-output theory, the microwave response of the cavity is modulated by Hamiltonian (1), yielding a microwave reflection amplitude of

$$S_{11} = -1 + \frac{\kappa_{ext}}{i(\omega_r - \omega_p) + g_1 \chi_1 + g_2 \chi_2 + \kappa_{tot}/2}, \quad (3)$$

where $\chi_i = \frac{g_i}{i(\omega_{a,i} - \omega_p) + \gamma_i}$ is the single-electron electric susceptibility, and γ_i is the decoherence rate of qubit i (34, 46).

We first examine the coupling between DQD 1 and the resonator. Here DQD 2 is detuned far away from

the resonator frequency, so that its interaction with the resonator can be neglected. The charge stability diagram of DQD 1 is detected using the microwave cavity by fixing the probe frequency at the resonator frequency $f_p = f_r = 6.48$ GHz, so that Eq. (3) can be simplified to $S_{11} = -1 + \frac{\kappa_{ext}}{g_1\chi_1 + \kappa_{tot}/2}$. The contribution from qubit 1, $g_1\chi_1$, will change the microwave response, with a particularly enhanced signal when the probe is near resonance with the qubit ($f_{a,1} \sim f_r = f_p$).

Figs. 2A and 2B show two different scenarios with $2t_1 = 6.55$ GHz and $2t_1 = 5.90$ GHz, respectively. In Fig. 2A, where $2t_1 = 6.55$ GHz $> f_r$, the qubit transition frequency is always larger than the resonator frequency no matter what δ_1 is. $\omega_{a,i} - \omega_p$ is minimum at $\delta_1 = 0$, thus maximizing $|S_{11}|$ at $\delta_1 = 0$ and resulting in a single transition line in the charge stability diagram. Hence, in Fig. 2C, there exists only one peak when we cut a line along the detuning of qubit 1 [white arrow in Fig. 2A]. On the other hand, when $2t_1 = 5.9$ GHz $< f_r$, $|g_1\chi_1|$ reaches its maximum at $\delta_1 = \pm\sqrt{(f_r)^2 - (2t_1)^2}$, where $\omega_{a,i} - \omega_p = 0$, leading to two transition lines in Fig. 2B, and Fig. 2D shows two separated peaks. Likewise, we can perform the same study of coupling between DQD 2 and the resonator, and observe similar results.

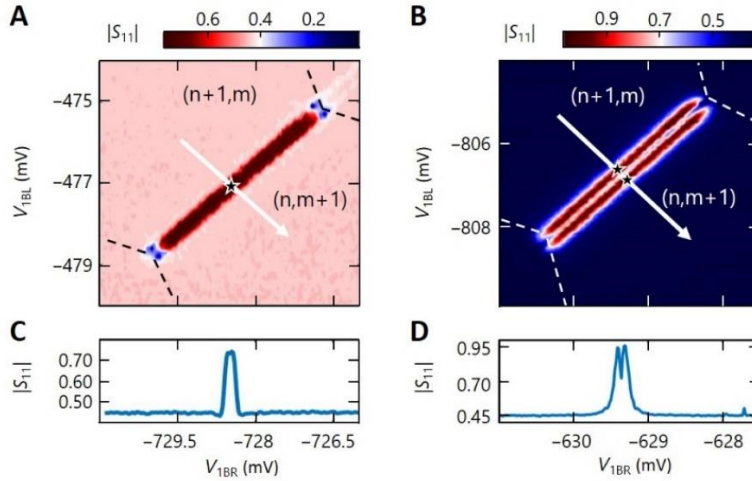


Fig. 2. Electron hexagonal charge stability diagrams of DQD 1 extracted from the reflected microwave amplitude $|S_{11}|$. The numbers (n, m) denote the charge number in the left and right dots, respectively. Measured $|S_{11}|$ as a function of V_{1BL} and V_{1BR} at (A) $2t_1 = 6.55$ GHz $> f_r$ and (B) $2t_1 = 5.90$ GHz $< f_r$. (C and D) are the cut lines along with the white arrows in (A) and (B), respectively. The black stars in (a) and (b) are used to illustrate the position of the peaks in (C) and (D).

Now that we have established how individual qubits couple to the resonator, we are ready to investigate nonlocal coherent coupling between the qubits mediated by the resonator. Earlier experiments have shown that coupled qubits can be resolved via enhanced Rabi splitting in the frequency domain, specifically by sweeping the probe microwave frequency (23, 42, 43). Here we adopt a different approach: we fix the probe frequency on resonance with the resonator, $\omega_p = \omega_r$, then investigate the nonlocal coherent coupling by measuring and analyzing the correlated two-qubit spectra as a function of the detuning of each qubit. Compared with commonly used microwave spectroscopy with probe frequency sweeps, our electrical tuning method is a more natural and convenient approach for semiconductor DQDs that are directly controlled by the gate voltages. Such sweeps of voltage detuning of the qubits allow us to explore the coupled qubits in a

broad range of system parameters quickly. Furthermore, by choosing the probe frequency to be resonant with the resonator, we have removed the extraneous contribution of probe-resonator mismatch from the microwave response in Eq. (3), and singled out the qubit contributions $g_i\chi_i$. Therefore, Eq. (3) can now be simplified as:

$$S_{11}(\delta_1, \delta_2) = -1 + \frac{\kappa_{ext}}{g_1\chi_1 + g_2\chi_2 + \kappa_{tot}/2}. \quad (4)$$

This expression explicitly illustrates the modulation caused by the coupling strengths g_i , which are in turn determined by the tunnel coupling rate $2t_i$ of DQD i .

Parametrized by the relative strength of the tunnel coupling rate of DQD i and the resonator frequency, there are nine different coupling regimes. To prevent repetition, and without loss of generality, we now focus on the behaviors and evolutions of the correlated spectra of four characteristic coupling regimes by varying the tunnel coupling $(2t_1, 2t_2)$ of the two qubits.

(i) For $(2t_1, 2t_2) = (6.65, 6.76)$ GHz $> f_r$, as shown in Fig. 3A, a red crossed pattern with a deep red center intuitively shows that $|S_{11}|$ increases as $|\delta_i|$ decreases and is maximum at $|\delta_1| = |\delta_2| = 0$. In this regime in which both qubits are weakly coupled with the resonator, the qubits' contributions can be regarded as a shift of the resonator frequency $\Delta\omega_r = \mathbf{Im}\{g_1\chi_1 + g_2\chi_2\}$, resulting in the change in $|S_{11}|$ around $|\delta_1| = |\delta_2| = 0$ being almost a linear superposition of responses from individual qubits (34, 47).

(ii) For $(2t_1, 2t_2) = (6.48, 6.76)$ GHz, so that $2t_1 = f_r < 2t_2$, as shown in Fig. 3B, the single peak in the central area of Fig. 3A is split into two peaks that lie symmetrically on either side of $\delta_1 = 0$. In the central area where $g_1\chi_1 \gg g_2\chi_2$, the contribution of qubit 1 is much larger than that of qubit 2 and plays the leading role in the microwave response. However, qubit 2 does modify the signal, leading to the two peaks being extended out, as illustrated in the center of Fig. 3B.

(iii) For $2t_1 = 2t_2 = f_r = 6.48$ GHz, the qubits are operating in the strong coupling limit. From Eq. (4), $g_i\chi_i$ will dominate the microwave response when $g_i \sim g_i^{max}$, especially if $g_i\chi_i$ is greater than $\frac{\kappa_i + \kappa_e}{2}$.

This is the limit when the two qubits and the resonator are completely mixed, which leads to an interesting pattern in Fig. 3C. In particular, in the central area, the enhanced reflection extends outward along the diagonal lines, where the two qubits become detuned from the resonator but are still resonant with each other with $f_{a,1} = f_{a,2}$, resulting in a distinct X-like pattern in the reflection signal. The two qubits are the most strongly coupled via the resonator along the diagonals, with an effective coupling strength $g_{eff} = \sqrt{g_1^2 + g_2^2}$. Consequently, the enhanced reflection signal is detected in an X-like pattern extending along both diagonal directions.

(iv) Finally, with the DQD's tunnel coupling tuned away from $t_1 = 6.48$ GHz to $t_1 = 6.42$ GHz, which means that $2t_1 < 2t_2 = f_r$, the X-like pattern is stretched in the horizontal (δ_1) direction in Fig. 3D. Basically, to maintain qubit resonance with each other, larger δ_1 is needed because of the smaller t_1 . The single enhanced peak in the central area of Fig. 3C splits into two peaks at the corresponding detuning points $\delta_1 = \pm\sqrt{f_r^2 - (2t_1)^2}$, where $f_{a,1} = f_r$ in Fig. 3D. The additional two light valley spots, caused by the phase-cancellation between the two qubits (see Supplementary Materials), appear on the sides of the X-axis around $\delta_1 = 0$. Similarly, when both tunnel couplings are tuned small than f_r , another two spots of reduced reflection will appear on the sides of the Y-axis around $\delta_2 = 0$.

The top panels in Fig. 3 show that by scanning the gate voltages for the two qubits, the geometrical

patterns in different coupling regimes exhibit unique features that intuitively provide information about the frequency relationships among the resonator and the two qubits. To confirm this point, we simulate these correlated spectra using averaged typical parameters of $(g_1^{max}, g_2^{max}, \gamma_1, \gamma_2)/2\pi = (86, 85, 22, 23)$ MHz from (37, 42) with their corresponding tunnel coupling rates. The simulated correlated spectra, shown in Fig. 3 (E to H), qualitatively profile our intriguing experimental evolutions very well. However, the color scale of the patterns does not match our experimental results quantitatively, since the input parameters are estimated typical values instead of the real values in our hybrid system. The more interesting question is whether these parameters can change the geometrical patterns and whether we can extract our system parameters from the experimentally established correlation spectrum.

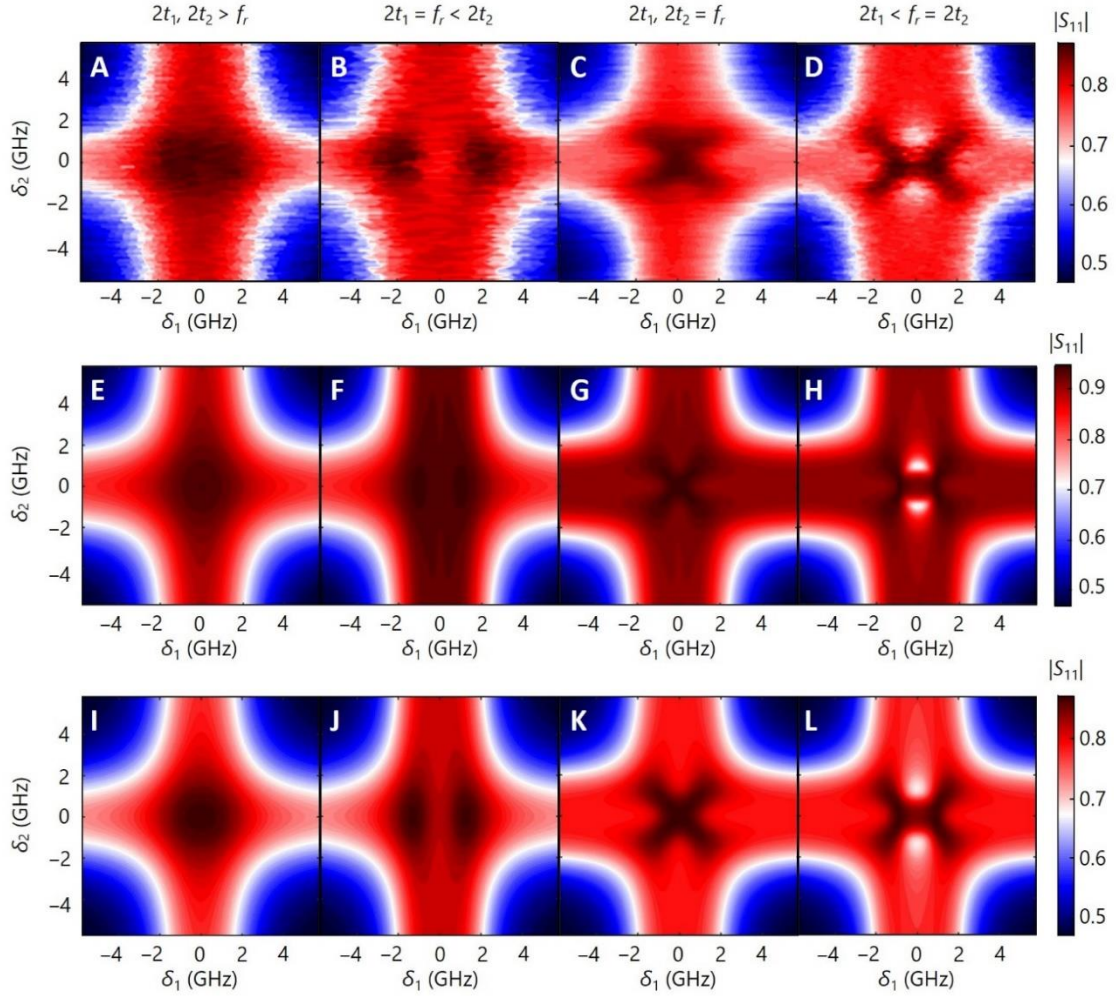


Fig. 3. Measured correlated spectra as a function of δ_1 and δ_2 with different $2t_1$ and $2t_2$ at $f_p = f_r = 6.48$ GHz. (A) $(2t_1, 2t_2) = (6.65, 6.76)$ GHz, (B) $(2t_1, 2t_2) = (6.48, 6.76)$ GHz, (C) $(2t_1, 2t_2) = (6.48, 6.48)$ GHz, and (D) $(2t_1, 2t_2) = (6.42, 6.48)$ GHz. Calculations of the two-qubit correlated spectra with input-output theory in the TC model corresponding to (A) ~ (D) with typical parameters of $(g_1^{max}, g_2^{max}, \gamma_1, \gamma_2)/2\pi = (86, 85, 22, 23)$ MHz and extracted parameters of $(g_1^{max}, g_2^{max}, \gamma_1, \gamma_2)/2\pi = (75, 75, 50, 50)$ MHz are shown in (E to H) and (I to L) respectively .

To understand the dependence of the spectrum patterns on the parameters $(g_1^{max}, g_2^{max}, \gamma_1, \gamma_2)/2\pi$

quantitatively, we focus on the geometric features of the X-like pattern in Fig. 3C, where each qubit is at or near its maximum coupling strength g_i^{max} , and systematically investigate its evolution theoretically. Since both qubits are fabricated on the same wafer, confined using the same structure and operating in the same environment, we take $\gamma_1 = \gamma_2 = \gamma$ for simplicity without loss of generality. Here, we use a few typical parameters to characterize the features of the X-like pattern. The first parameter is the ratio $\delta_1^{FHW M} / \delta_2^{FHW M}$, where $\delta_{1(2)}^{FHW M}$ is the full width at half maximum (FWHM) along the X(Y)-axis, as shown in Fig. 4A. Fig. 4B shows the calculated results of $\log_2(\delta_1^{FHW M} / \delta_2^{FHW M})$ as a function of $g_1^{max} / 2\pi$ and $g_2^{max} / 2\pi$. From the contour line in Fig. 4B, it is clearly seen that $\log_2(\delta_1^{FHW M} / \delta_2^{FHW M})$ is almost linearly related to the ratio of g_1^{max} / g_2^{max} . Combined with our experimental data $\delta_1^{FHW M} / \delta_2^{FHW M} = 0.99$ extracted from Fig. 3C, we can estimate that $g_1^{max} / g_2^{max} \approx 1$, i.e., $g_1^{max} \approx g_2^{max} = g$.

We then take a line cut along the off-diagonal $\delta_1 = \delta_2$ in Fig. 4A and use $\delta_{12}^{FHW M}$ and $|S_{11}|^{max}$ to denote the FWHM and maximum value of the curve, respectively. The calculated result of the FWHM as a function of $g / 2\pi$ and $\gamma / 2\pi$ shown in Fig. 4C indicates that $\delta_{12}^{FHW M}$ is almost completely determined by the coupling rate $g / 2\pi$ and is insensitive to the dephasing rate $\gamma / 2\pi$. Therefore, using the value $\delta_{12}^{FHW M} = 5.96$ GHz extracted from the experimental data in Fig. 3C, we obtain the coupling strength $g / 2\pi = 75$ MHz. The relationship between $|S_{11}|^{max}$ and $g / 2\pi$ and $\gamma / 2\pi$ is more complex, as shown in Fig. 4D, which presents the evolution of $|S_{11}|^{max}$ as a function of the coupling rate g and decoherence rate γ . However, combined with the estimated coupling rate $g / 2\pi = 75$ MHz and the experimental value $|S_{11}|^{max} = 0.89$, $\gamma / 2\pi = 50$ MHz can also be determined through Fig. 4D. To further verify our analysis, we compare the experimental curve and calculation results of $|S_{11}|^{max}$ for different parameters. Fig. 4E shows that if we change either g or γ from our estimated values, the calculated curve of $|S_{11}|^{max}$ will deviate from the experimental result, thus verifying the validity of our analysis and estimate.

As stated above, with the help of theoretical analysis, all the typical parameters of our hybrid system can indeed be estimated through an analysis of the correlated spectra. The estimated parameters $(g_1^{max}, g_2^{max}, \gamma_1, \gamma_2) / 2\pi = (75, 75, 50, 50)$ MHz are consistent with those of early experiments. Using the estimated parameters, the correlated spectrum of $2t_1 = 2t_2 = f_r = 6.48$ GHz is well reproduced with input-output theory, as shown in Fig. 4A. The other experimental correlated spectra for different parameter regimes in Fig. 3 (A to D) have also been simulated in Fig.3 (I to L). The calculated spectra in different working regimes not only qualitatively describe our experimental intriguing evolutions very well, but also reproduced the color scale of the patterns quantitatively. This method can also be used in different coupling regimes, and the relevant conclusions are shown in the Supplementary Materials.

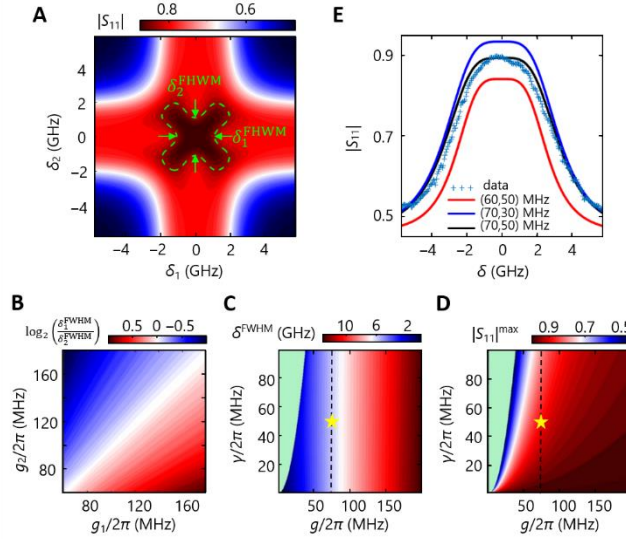


Fig. 4. Geometric features of the X-like pattern. (A) Simulated two-qubit correlated spectrum corresponding to Fig. 3C with the parameters of $(g_1^{max}, g_2^{max}, \gamma_1, \gamma_2)/2\pi = (75, 75, 50, 50)$ MHz. (B) The ratio of δ_1^{FWHM} to δ_2^{FWHM} as a function of g_1^{max} and g_2^{max} (C and D) The FWHM and $|S_{11}|^{max}$ are as a function of the coherence rate $g = g_1 = g_2$ and decoherence rate $\gamma = \gamma_1 = \gamma_2$. The yellow star refers to the parameters $(g_1^{max}, g_2^{max}, \gamma_1, \gamma_2)/2\pi = (75, 75, 50, 50)$ MHz. The green region refers to the regime in which the X-like pattern disappears where both qubits are weakly coupled with the resonator. (E) $|S_{11}|$ as a function of $\delta_1 = \delta_2$ at $2t_1 = 2t_2 = f$. The sky-blue crosses are the data along the black dashed line in Fig. 3C. The red, blue and black lines are simulated with different values of $(g, \gamma)/2\pi$.

CONCLUSION

In conclusion, we have investigated the correlation of two microwave-photon-coupled qubits with a new spectroscopy method. From the distinguishing patterns in the qubit detuning space, resonant coupling between either of the qubits and the resonator can be quickly identified. By analyzing the geometric features of the correlated spectra when the tunnel coupling of both qubits is equal to the resonator frequency, we can further estimate a set of parameters for the hybrid system. The observed patterns are in excellent agreement with the simulation of the TC model using the extracted parameters. The correlated spectroscopy method introduced here quickly and intuitively characterizes pairwise interactions of two distant semiconductor qubits via microwave photons and could potentially be expanded as a practical method to quickly characterize multiple cavity QED coupled qubits in other system.

MATERIALS AND METHODS

The device we studied here was fabricated on the GaAs/AlGaAs heterostructure, with the two-dimensional electron gas (2DEG) about 90nm below the heterostructure surface. The SQUID array, which consists of 34 Al/AIO_x/Al Josephson Junction loops, was fabricated using suspended bridge method and double angle shadow evaporation. The 2DEG under the resonator area was etched away to reduce the microwave leakage. The double quantum dot is confined by electrostatic potential applied on Ti/Au metal gates which were fabricated through UV lithography and electron beam lithography.

SUPPLEMENTARY MATERIALS

Section S1. Crosstalk between the nonlocal two qubits

Section S2. The microwave response in different regimes

Section S3. Geometric features of the separated peaks in Fig. 3A

Section S4. Geometric features of the separated peaks in Fig. 3B

Section S5. Geometric features of the bright spots in Fig. 3D

Fig. S1. Voltage crosstalk between nonlocal two qubits.

Fig. S2. Microwave response of two qubits.

Fig. S3. Geometric features of the separated peaks.

Fig. S4. Geometric features of the bright spots.

REFERENCES

1. D. Loss, D. P. DiVincenzo, Quantum computation with quantum dots. *Phys. Rev. A* **57**, 120 (1998).
2. R. Hanson, L. P. Kouwenhoven, J. R. Petta, S. Tarucha, L. M. K. Vandersypen, Spins in few-electron quantum dots. *Rev. Mod. Phys.* **79**, 1217-1265 (2007).
3. F. A. Zwanenburg, A. S. Dzurak, A. Morello, M. Y. Simmons, L. C. L. Hollenberg, G. Klimeck, S. Rogge, S. N. Coppersmith, M. A. Eriksson, Silicon quantum electronics. *Rev. Mod. Phys.* **85**, 961-1019 (2013).
4. G. Cao, H.-O. Li, T. Tu, L. Wang, C. Zhou, M. Xiao, G.-C. Guo, H.-W. Jiang, G.-P. Guo, Ultrafast universal quantum control of a quantum-dot charge qubit using Landau–Zener–Stückelberg interference. *Nat. Commun.* **4**, 1401 (2013).
5. H.-O. Li, G. Cao, G.-D. Yu, M. Xiao, G.-C. Guo, H.-W. Jiang, G.-P. Guo, Conditional rotation of two strongly coupled semiconductor charge qubits. *Nat. Commun.* **6**, 7681 (2015).
6. H.-O. Li, G. Cao, G.-D. Yu, M. Xiao, G.-C. Guo, H.-W. Jiang, G.-P. Guo, Controlled quantum operations of a semiconductor three-qubit system. *Phys. Rev. Appl.* **9**, 024015 (2018).
7. B.-C. Wang, G. Cao, H.-O. Li, M. Xiao, G.-C. Guo, X. Hu, H.-W. Jiang, G.-P. Guo, Tunable hybrid qubit in a triple quantum dot. *Phys. Rev. Appl.* **8**, 064035 (2017).
8. G. Cao, H.-O. Li, G.-D. Yu, B.-C. Wang, B.-B. Chen, X.-X. Song, M. Xiao, G.-C. Guo, H.-W. Jiang, X. Hu, G.-P. Guo, Tunable hybrid qubit in a GaAs double quantum dot. *Phys. Rev. Lett.* **116**, 086801 (2016).
9. D. Kim, Z. Shi, C. Simmons, D. Ward, J. Prance, T. S. Koh, J. K. Gamble, D. Savage, M. Lagally, M. Friesen, S. N. Coppersmith, M. A. Eriksson, Quantum control and process tomography of a semiconductor quantum dot hybrid qubit. *Nature* **511**, 70 (2014).
10. J. R. Petta, A. C. Johnson, J. M. Taylor, E. A. Laird, A. Yacoby, M. D. Lukin, C. M. Marcus, M. P. Hanson, A. C. Gossard, Coherent manipulation of coupled electron spins in semiconductor quantum dots. *Science* **309**, 2180-2184 (2005).
11. F. H. L. Koppens, C. Buizert, K.-J. Tielrooij, I. T. Vink, K. C. Nowack, T. Meunier, L. P. Kouwenhoven, L. M. K. Vandersypen, Driven coherent oscillations of a single electron spin in a quantum dot. *Nature* **442**, 766 (2006).

12. M. D. Shulman, O. E. Dial, S. P. Harvey, H. Bluhm, V. Umansky, A. Yacoby, Demonstration of entanglement of electrostatically coupled singlet-triplet qubits. *Science* **336**, 202-205 (2012).
13. M. Xiao, I. Martin, E. Yablonovitch, H.-W. Jiang, Electrical detection of the spin resonance of a single electron in a silicon field-effect transistor. *Nature* **430**, 435 (2004).
14. B. M. Maune, M. G. Borselli, B. Huang, T. D. Ladd, P. W. Deelman, K. S. Holabird, A. A. Kiselev, I. Alvarado-Rodriguez, R. S. Ross, A. E. Schmitz, C. A. Watson, Coherent singlet-triplet oscillations in a silicon-based double quantum dot. *Nature* **481**, 344 (2012).
15. M. Veldhorst, C. H. Yang, J. C. C. Hwang, W. Huang, J. P. Dehollain, J. T. Muhonen, S. Simmons, A. Laucht, F. E. Hudson, K. M. Itoh, A. Morello, A. S. Dzurak, A two-qubit logic gate in silicon. *Nature* **526**, 410 (2015).
16. Y. He, S. K. Gorman, D. Keith, L. Kranz, J. G. Keizer, M. Y. Simmons, A two-qubit gate between phosphorus donor electrons in silicon. *Nature* **571**, 371-375 (2019).
17. W. Huang, C. H. Yang, K. W. Chan, T. Tanttu, B. Hensen, R. C. C. Leon, M. A. Fogarty, J. C. C. Hwang, F. E. Hudson, K. M. Itoh, A. Morello, A. Laucht, A. S. Dzurak, Fidelity benchmarks for two-qubit gates in silicon. *Nature* **569**, 532 (2019).
18. T. F. Watson, S. G. J. Philips, E. Kawakami, D. R. Ward, P. Scarlino, M. Veldhorst, D. E. Savage, M. G. Lagally, M. Friesen, S. N. Coppersmith, M. A. Eriksson, L. M. K. vandersypen, A programmable two-qubit quantum processor in silicon. *Nature* **555**, 633 (2018).
19. D. M. Zajac, A. J. Sigillito, M. Russ, F. Borjans, J. M. Taylor, G. Burkard, J. R. Petta, Resonantly driven CNOT gate for electron spins. *Science* **359**, 439-442 (2018).
20. J. Yoneda, K. Takeda, T. Otsuka, T. Nakajima, M. R. Delbecq, G. Allison, T. Honda, T. Kodera, S. Oda, Y. Hoshi, N. U. Usami, S. Tarucha, A quantum-dot spin qubit with coherence limited by charge noise and fidelity higher than 99.9%. *Nat. Nano.* **13**, 102 (2018).
21. G. Shinkai, T. Hayashi, T. Ota, T. Fujisawa, Correlated coherent oscillations in coupled semiconductor charge qubits. *Phys. Rev. Lett.* **103**, 056802 (2009).
22. D. R. Ward, D. Kim, D. E. Savage, M. G. Lagally, R. H. Foote, M. Friesen, S. N. Coppersmith, M. A. Eriksson, State-conditional coherent charge qubit oscillations in a Si/SiGe quadruple quantum dot. *npj Quant. Inf.* **2**, 16032 (2016).
23. J. Majer, J. M. Chow, J. M. Gambetta, J. Koch, B. R. Johnson, J. A. Schreier, L. Frunzio, D. I. Schuster, A. A. Houck, A. Wallraff, Coupling superconducting qubits via a cavity bus. *Nature* **449**, 443-447 (2007).
24. M. A. Sillanpää, J. I. Park, R. W. Simmonds, Coherent quantum state storage and transfer between two phase qubits via a resonant cavity. *Nature* **449**, 438 (2007).
25. T. Astner, S. Nevlacsil, N. Peterschofsky, A. Angerer, S. Rotter, S. Putz, J. Schmiedmayer, J. Majer, Coherent coupling of remote spin ensembles via a cavity bus. *Phys. Rev. Lett.* **118**, 140502 (2017).
26. A. Wallraff, D. I. Schuster, A. Blais, L. Frunzio, J. Majer, M. H. Devoret, S. M. Girvin, R. J. Schoelkopf, Approaching unit visibility for control of a superconducting qubit with dispersive readout. *Phys. Rev. Lett.* **95**, 060501 (2005).
27. D. I. Schuster, A. Wallraff, A. Blais, L. Frunzio, R. S. Huang, J. Majer, S. M. Girvin, R. J. Schoelkopf, ac Stark shift and dephasing of a superconducting qubit strongly coupled to a cavity field. *Phys. Rev. Lett.* **94**, 123602 (2005).

28. P. Scarlino, D. J. Van Woerkom, A. Stockklauser, J. V. Koski, M. C. Collodo, S. Gasparinetti, C. Reichl, W. Wegscheider, T. Ihn, K. Ensslin, All-microwave control and dispersive readout of gate-defined quantum dot qubits in circuit quantum electrodynamics. *Phys. Rev. Lett.* **122**, 206802 (2019).
29. J. Q. You, F. Nori, Atomic physics and quantum optics using superconducting circuits. *Nature* **474**, 589 (2011).
30. T. Frey, P. J. Leek, M. Beck, A. Blais, T. Ihn, K. Ensslin, A. Wallraff, Dipole Coupling of a Double Quantum Dot to a Microwave Resonator. *Phys. Rev. Lett.* **108**, 046807 (2012).
31. L. E. Bruhat, J. J. Viennot, M. C. Dartiailh, M. M. Desjardins, T. Kontos, A. Cottet, Cavity photons as a probe for charge relaxation resistance and photon emission in a quantum dot coupled to normal and superconducting continua. *Phys. Rev. X* **6**, 021014 (2016).
32. Y.-Y. Liu, K. D. Petersson, J. Stehlik, J. M. Taylor, J. R. Petta, Photon emission from a cavity-coupled double quantum dot. *Phys. Rev. Lett.* **113**, 036801 (2014).
33. K. D. Petersson, L. W. McFaul, M. D. Schroer, M. Jung, J. M. Taylor, A. A. Houck, J. R. Petta, Circuit quantum electrodynamics with a spin qubit. *Nature* **490**, 380 (2012).
34. G.-W. Deng, D. Wei, S.-X. Li, J. R. Johansson, W.-C. Kong, H.-O. Li, G. Cao, M. Xiao, G.-C. Guo, F. Nori, H.-W. Jiang, G.-P. Guo, Coupling Two Distant Double Quantum Dots with a Microwave Resonator. *Nano Lett.* **15**, 6620 (2015).
35. J. Viennot, M. Dartiailh, A. Cottet, T. Kontos, Coherent coupling of a single spin to microwave cavity photons. *Science* **349**, 408-411 (2015).
36. X. Hu, Y.-x. Liu, F. Nori, Strong coupling of a spin qubit to a superconducting stripline cavity. *Phys. Rev. B* **86**, 035314 (2012).
37. A. Stockklauser, P. Scarlino, J. V. Koski, S. Gasparinetti, C. K. Andersen, C. Reichl, W. Wegscheider, T. Ihn, K. Ensslin, A. Wallraff, Strong Coupling Cavity QED with Gate-Defined Double Quantum Dots Enabled by a High Impedance Resonator. *Phys. Rev. X* **7**, 011030 (2017).
38. X. Mi, J. V. Cady, D. M. Zajac, P. W. Deelman, J. R. Petta, Strong coupling of a single electron in silicon to a microwave photon. *Science* **355**, 156-158 (2017).
39. X. Mi, M. Benito, S. Putz, D. M. Zajac, J. M. Taylor, G. Burkard, J. R. Petta, A coherent spin–photon interface in silicon. *Nature* **555**, 599-603 (2018).
40. N. Samkharadze, G. Zheng, N. Kalhor, D. Brousse, A. Sammak, U. C. Mendes, A. Blais, G. Scappucci, L. M. K. Vandersypen, Strong spin-photon coupling in silicon. *Science* **359**, 1123-1127 (2018).
41. A. J. Landig, J. V. Koski, P. Scarlino, U. Mendes, A. Blais, C. Reichl, W. Wegscheider, A. Wallraff, K. Ensslin, T. Ihn, Coherent spin–photon coupling using a resonant exchange qubit. *Nature* **560**, 179 (2018).
42. D. J. van Woerkom, P. Scarlino, J. H. Ungerer, C. Müller, J. V. Koski, A. J. Landig, C. Reichl, W. Wegscheider, T. Ihn, K. Ensslin, A. Wallraff, Microwave Photon-Mediated Interactions between Semiconductor Qubits. *Phys. Rev. X* **8**, 041018 (2018).
43. F. Borjans, X. G. Croot, X. Mi, M. J. Gullans, J. R. Petta, Resonant microwave-mediated interactions between distant electron spins. *Nature* **577**, 195-198 (2020).
44. M. Tavis, F. W. Cummings, Exact solution for an N-molecule—radiation-field Hamiltonian. *Phys. Rev.* **170**, 379 (1968).

45. L. Childress, A. S. Sørensen, M. D. Lukin, Mesoscopic cavity quantum electrodynamics with quantum dots. *Phys. Rev. A* **69**, 042302 (2004).
46. G. Burkard, M. J. Gullans, X. Mi, J. R. Petta, Superconductor-semiconductor hybrid cavity quantum electrodynamics. *arXiv: 1905.01155* (2019).
47. M. R. Delbecq, L. E. Bruhat, J. J. Viennot, S. Datta, A. Cottet, T. Kontos, Photon-mediated interaction between distant quantum dot circuits. *Nat. Commun.* **4**, 1400 (2013).

Acknowledgments:

This work was supported by the National Key Research and Development Program of China (Grant No.2016YFA0301700), the National Natural Science Foundation of China (Grants No. 61922074, 11674300, 61674132, 11625419 and 11804327), the Strategic Priority Research Program of the CAS (Grant Nos. XDB24030601), the Anhui initiative in Quantum Information Technologies (Grants No. AHY080000). H.-W. J. and X. H. acknowledge financial support by U.S. ARO through Grant No. W911NF1410346 and No. W911NF1710257, respectively. This work was partially carried out at the University of Science and Technology of China Center for Micro and Nanoscale Research and Fabrication.

Author Contributions:

B.-C.W., H.-O.L., S.-S.G. fabricated the sample. B.-C.W., H.-O.L., T.L., and G.C. performed the measurements and ran simulations. T. L., G.C., M.-B.C., X.H., H.-W.J. and G.-P.G. analyzed the data. G.-C.G. and G.-P.G. advised on experiments and data analysis. G.P.G. and C.G. supervised the experiments. All authors contributed to write the paper.

Competing interests:

The authors declare that they have no competing interests.

Data and materials availability:

All data needed to evaluate the conclusions in the paper are present in the paper and/or the Supplementary Materials. Additional data related to this paper may be requested from the authors.

Supplemental Material: Correlated spectrum of distant semiconductor qubits coupled by microwave photons

Section S1. Crosstalk between the nonlocal two qubits

In our sample structure, the two plunger gates 1PR and 2PL connect with each other via the SQUID array resonator. In order to determine the influence of capacitive coupling between the two qubits, we measure the crosstalk of our hybrid system. Since the plunger Gates 1PR and 2PL are floated without bias voltages, here we scan voltages on Gate 1BR (close to Gate 1PR) and Gate 2BL (close to Gate 2PL) to detect maximum crosstalk. In contrast, we scan voltages on Gate 1BL (far from Gate 1PR) and Gate 2BR (far from Gate 2PL) to detect minimum crosstalk.

As shown in Fig. S1A, microwave response is as a function of V_{2BL} and V_{1BR} , where V_{1BR} is scanned across the inter-dot transition line of Qubit 1. Two green dashed lines in Fig. S1A are the degenerate points between Qubit 1 and the resonator, since $2t_1 < f_r$. The slop of the dashed lines $k_1 \sim -1/215$ indicates the capacitive relationship of the two nonlocal qubits. In Fig. S1B, the capacitive relationship between Gates 2BR and 1BL is detected in the same way, predicting the slop of the dashed lines $k_2 \sim 0$. In our experiments in Fig. 3, the central regions of the correlated spectra are within the range of $|\delta_i| < 4$ GHz, corresponding to the shift of the other qubit is $|\delta_i| \cdot \max(|k_1|, |k_2|) < 19$ MHz. Hence, the effect of crosstalk between the two nonlocal qubits is ignored in our experiments.

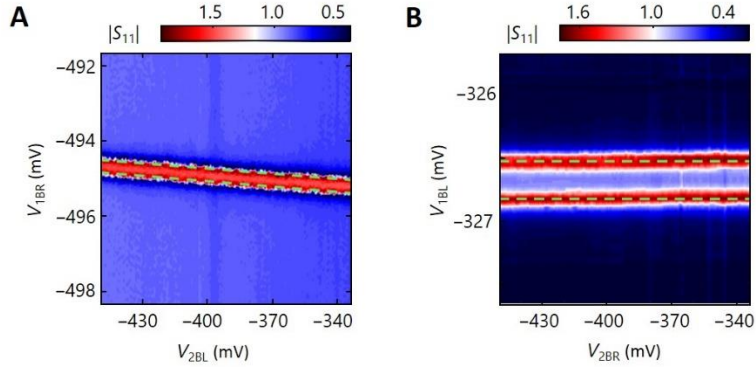


Fig. S1. Voltage crosstalk between nonlocal two qubits. (A) Measured $|S_{11}|$ as a function of V_{2BL} and V_{1BR} . (B) Measured $|S_{11}|$ as a function of V_{2BR} and V_{1BL} . (In (A) and (B), Qubit 1 has the same tunnel coupling rate $2t_1$.)

Section S2. The microwave response in different regimes

In the main text, we studied the evolutions of correlated spectra in different coupling regimes by varying the tunnel coupling $(2t_1, 2t_2)$ of the two qubits, and describe the behaviors qualitatively. Here we analyze the correlated spectra quantitatively by using the equation

$$S_{11}(\delta_1, \delta_2) = -1 + \frac{\kappa_{ext}}{g_1\chi_1 + g_2\chi_2 + \kappa_{tot}/2}. \quad (S1)$$

(i) For $(2t_1, 2t_2) = (6.65, 6.76)$ GHz $> f_r$. Qubit contributions $g_i\chi_i$ in Eq. (S1) is a small amount compared with the microwave loss $\kappa_{tot}/2$ via the resonator in this regime. By expanding Eq. (S1) to the first order of $g_i\chi_i$, we get $S_{11}(\delta_1, \delta_2) \approx -1 + \frac{2\kappa_{ext}}{\kappa_{tot}} \left(1 - \frac{g_1\chi_1 + g_2\chi_2}{\kappa_{tot}/2}\right)$, which predicts that the change of microwave reflectance is proportional to the sum of $|g_1\chi_1|$ and $|g_2\chi_2|$, as shown in Fig. 3A.

(ii) For $(2t_1, 2t_2) = (6.48, 6.76)$ GHz. In this working regime, the contribution of Qubit 1 is much larger than that of Qubit 2 and plays the leading role for the microwave response. However, $g_2\chi_2 \approx -ig_2^2/\Delta_2$ provides an external imaginary ($\Delta_i = \omega_i - \omega_p = \omega_i - \omega_r$, $\omega_{a,i}/2\pi = \sqrt{\delta_i^2 + (2t_i)^2}$), and the Eq. (S1) can be written as $S_{11} \approx -1 + \frac{\kappa_{ext}}{(g_1\chi_1 + \kappa_{tot}/2)e^{i\theta}}$ around $\Delta_1 = 0$, where $\theta = -\arctan(\frac{g_2^2/\Delta_2}{g_1\chi_1 + \kappa_{tot}/2})$ is the factor to describe the asymmetry caused by Qubit 2. In Fig. 3B, with Qubit 2 is far detuned from Qubit 1 and the resonator, $\theta \approx 0$ and the microwave reflectance $S_{11} = -1 + \frac{\kappa_{ext}}{g_1\chi_1 + \kappa_{tot}/2}$ maximizes at $\Delta_1 = 0$ ($\delta_1 = 0$). As $|\delta_2|$ decreases, the increased $|\theta|$ modifies the signal, resulting in the enhancement of the peaks' value at larger Δ_1 ($|\delta_1|$), i.e., the separated peaks extended out around $|\delta_2| = 0$.

(iii) For $2t_1 = 2t_2 = f_r = 6.48$ GHz. In the central area, $g_2\chi_2$ is on the same order of magnitude as $g_1\chi_1$. When $\Delta_2(|\delta_2|)$ is detuned from 0, $g_2\chi_2 = \frac{g_2^2}{i\Delta_2 + \gamma_2}$ provides an external imaginary part which is 0 at $\Delta_2(|\delta_2|) = 0$ and increases within $\Delta_2 < \gamma_2$. Thus the separated peaks at the cut line along the detuning of Qubit 1 arise and extend out at the cut lines as $\Delta_2(|\delta_2|)$ increases. Likewise, we observe the separated peaks at the cut lines along the detuning of Qubit 2.

(iv) For $2t_1 = 6.42$ GHz $< f_r = 2t_2 = 6.48$ GHz. If we only consider the interaction between Qubit 2 and the resonator and measure the microwave reflectance $|S_{11}|$ as a function of $\Delta_2(\delta_2)$, there will exist only one peak. The qubit part $|g_2\chi_2| = \frac{g_2^2}{\sqrt{\gamma_2^2 + \Delta_2^2}}$ maximizes at $\Delta_2 = 0$ ($\delta_2 = 0$) and decrease monotonically as $|\Delta_2|$ ($|\delta_2|$) increasing. However, differ from Fig.2A, in this working regime, Qubit 1's inter-dot tunneling rate $2t_1$ is close to f_r and the coupling between Qubit 1 and the resonator provides an imaginary part which has the opposite sign compared with the imaginary part induced by Qubit 2. Thus, the set-off between two qubits is conspicuous around $(\delta_1, \delta_2) \sim (0, 1.5)$ GHz in Fig. 3D.

Section S3. Geometric features of the separated peaks in Fig. 3A

For $(2t_1, 2t_2) = (6.65, 6.76)$ GHz $> f_r$. As we discussed in Section III, with both qubits far detuned from f_r , qubit contributions $g_i\chi_i$ in Eq. (S1) is a small amount compared with the resonator loss $\kappa_{tot}/2$ via the resonator in this regime. With the interaction between resonator and qubits, the reflectance is enhanced by $\Delta|S_{11}|$ at $\delta_1 = \delta_2 = 0$. Fig. S2 shows that the change of microwave reflectance $\Delta|S_{11}|$ as a function of g_1^{max} and g_2^{max} . And in the weak coupling regime where $g_1^{max}, g_2^{max} \ll \gamma = 50$ MHz, the calculated result conform to the simplified equation $S_{11}(\delta_1, \delta_2) \approx -1 + \frac{2\kappa_{ext}}{\kappa_{tot}} (1 - \frac{g_1\chi_1 + g_2\chi_2}{\kappa_{tot}/2})$, predicting that the change of microwave reflectance is proportional to the sum of $|g_1\chi_1|$ and $|g_2\chi_2|$.

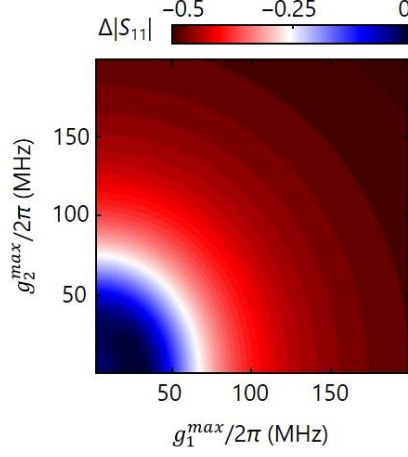


Fig. S2. Microwave response of two qubits. $\Delta|S_{11}|$ as function of g_1^{max} and g_2^{max}

Section S4. Geometric features of the separated peaks in Fig. 3B

In Fig. 3B of the main text, with $2t_1 = f_r = 6.48$ GHz and the inter-dot tunnel coupling rate of DQD 2 tuned to $2t_2 = 6.76$ GHz, two separated peaks symmetrically lie on the two sides of $\delta_1 = 0$. In this working regime ($|g_1\chi_1| \gg |g_2\chi_2|, \kappa_{tot}$), the contribution of Qubit 1 plays the leading role for the microwave response. However, with the modification of external imaginary of $g_2\chi_2$, the maximum value of microwave reflectance does not appear at $\delta_1 = \delta_2 = 0$, but locates at two different positions on the X-axis ($\delta_2 = 0$). Here we characterize the features of the separated peaks with δ_1^d and $|S_{11}|^{max}$, where δ_1^d is the distance between the two peaks along $\delta_2 = 0$ and $|S_{11}|^{max}$ is the value of peaks.

First, we investigate the evolutions of geometric features as a function of different (g, γ) . The calculated result in Fig. S3A predicts that the distance between two peaks δ_1^d increases as γ, g increasing. Fig. S3B shows that $|S_{11}|^{max}$ is enhanced with the increase of coupling rate g or the decrease of decoherence rate γ . Then, we calculate the dependence of the geometric features by changing (g_1^{max}, g_2^{max}) . In Fig. S3C, the distance between two peaks δ_1^d increases as g_2 increases. On the other hand, the microwave response is contributed from both qubits, the contribution of Qubit 2 is relatively weakened as g_1 increases, resulting in that two separated peaks approach each other and degenerate into a single one (green areas shown in Fig. S2 (C and D)). Fig. S3D shows that $|S_{11}|^{max}$, which is contributed by $g_1\chi_1$ and $g_2\chi_2$, is enhanced with the increase of g_1 and g_2 .

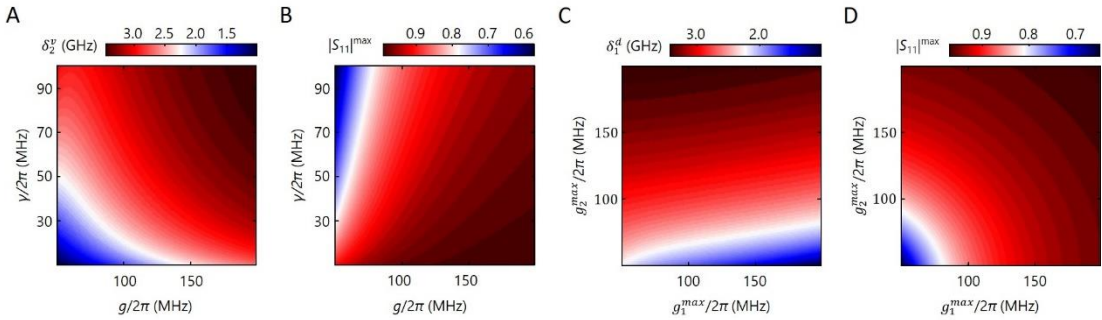


Fig. S3. Geometric features of the separated peaks. (A and B) δ_1^d and $|S_{11}|^{max}$ as function of coherence rate $g = g_1^{max} = g_2^{max}$ and decoherence rate $\gamma = \gamma_1 = \gamma_2$, respectively. (C and D) δ_1^d and $|S_{11}|^{max}$ as a function of g_1^{max} and g_2^{max}

Section S5. Geometric features of the bright spots in Fig. 3D

In Fig. 3D of the main text, with $2t_2 = f_r$ and the inter-dot tunnel coupling rate of DQD 1 tuned

from $2t_1 = 6.48$ GHz to $2t_1 = 6.42$ GHz, the two bright spots appear on the two sides of the X-axis around $\delta_1 = 0$. Within $|\delta_1| < \sqrt{f_r^2 - (2t_1)^2}$, the imaginary parts of $g_1\chi_1$ and $g_2\chi_2$ are different in positive and negative contributions in Eq. (3), so that the influences of the two qubits cancel out with each other, resulting in two dips of microwave reflectance. Here we characterize the features of the two bright spots with δ_2^v and C , where δ_2^v is the distance between two dips along $\delta_1 = 0$ and $C = \frac{|S_{11}(t_1, t_2=f_r) - S_{11}(t_1=f_r, t_2=f_r)|}{|S_{11}(t_1=f_r, t_2=f_r)|}$ is the relative change of the microwave reflectance compared to the case $2t_1 = 2t_2 = f_r$ at the corresponding position.

First, we investigate the evolutions of geometric features as a function of different (g, γ) . The calculated results in Fig. S4A show that the position of bright spots is nearly unchanged with the coupling rate g , and is detuned away from the center area as γ_2 increases. Fig. S4B predicts that the bright spots become more conspicuous as γ, g decreasing. Then we calculate the dependence of the geometric features on different $(g, 2t_1)$, shown in Fig. S4 (C and D). When $2t_1 \sim f_r = 6.48$ GHz, δ_2^v is almost infinity (not shown), corresponding to the situation that $g_1\chi_1$ provide a tiny imaginary part and $g_2\chi_2$ provide a negative one at a large δ_2 . However, $C \sim 0$ present it is not visible and we pay more attention to the observable set-off phenomenon in the experiment. With $2t_1$ decreasing and away from the resonance frequency, C increases significantly, i.e., the two bright spots become more conspicuous. So that the contrast of the bright spots can be considered as an outstanding feature to identify whether t_1 is getting close to f_r .

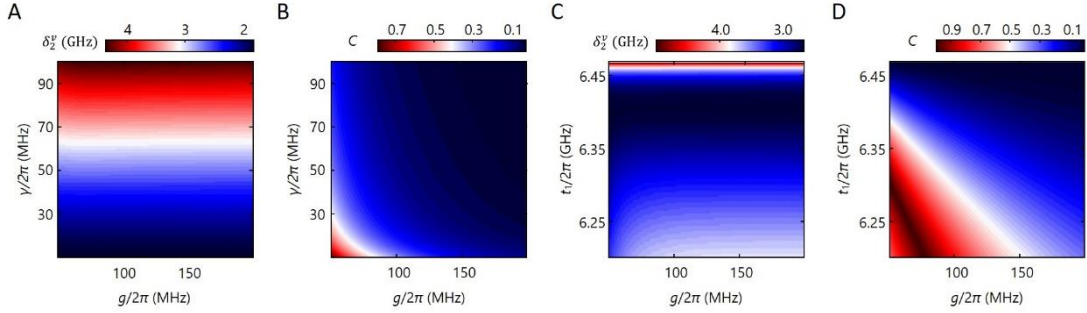


Fig. S4. Geometric features of the bright spots. (A and B) δ_2^v and C as function of coherence rate $g = g_1^{\max} = g_2^{\max}$ and decoherence rate $\gamma = \gamma_1 = \gamma_2$, respectively. (C and D) δ_2^v and C as a function of inter-dot tunnel coupling rate of DQD 1 coherence rate g and $2t_1$.